



# The Physical Origin of Dark Energy Constraints from Rubin Observatory and CMB-S4 Lensing Tomography

Byeonghee Yu,<sup>1</sup>  Simone Ferraro,<sup>2,1</sup>  Z Robert Knight,<sup>3</sup> Lloyd Knox,<sup>3</sup> Blake D. Sherwin<sup>4,5</sup>

<sup>1</sup>*Berkeley Center for Cosmological Physics, Department of Physics, University of California, Berkeley, CA 94720, USA*

<sup>2</sup>*Lawrence Berkeley National Laboratory, One Cyclotron Road, Berkeley, CA 94720, USA*

<sup>3</sup>*Physics Department, University of California, Davis, CA 95616, USA*

<sup>4</sup>*Department of Applied Mathematics and Theoretical Physics, University of Cambridge, Wilberforce Road, Cambridge CB3 0WA, UK*

<sup>5</sup>*Kavli Institute for Cosmology Cambridge, Madingley Road, Cambridge CB3 0HA, UK*

Accepted XXX. Received YYY; in original form ZZZ

## ABSTRACT

We seek to clarify the origin of constraints on the dark energy equation of state parameter from CMB lensing tomography, that is the combination of galaxy clustering and the cross-correlation of galaxies with CMB lensing in a number of redshift bins. In particular, we consider the two-point correlation functions which can be formed with a catalog of galaxy locations and photometric redshifts from the Vera C. Rubin Observatory Legacy Survey of Space and Time (LSST) and CMB lensing maps from the CMB-S4 experiment. We focus on the analytic understanding of the origin of the constraints. Dark energy information in these data arises from the influence of three primary relationships: distance as a function of redshift (geometry), the amplitude of the power spectrum as a function of redshift (growth), and the power spectrum as a function of wavenumber (shape). We find that the effects from geometry and growth play a significant role and partially cancel each other out, while the shape effect is unimportant. We also show that Dark Energy Task Force (DETF) Figure of Merit (FoM) forecasts from the combination of LSST galaxies and CMB-S4 lensing are comparable to the forecasts from cosmic shear in the absence of the CMB lensing map, thus providing an important independent check. Compared to the forecasts with the LSST galaxies alone, combining CMB lensing and LSST clustering information (together with the primary CMB spectra) increases the FoM by roughly a factor of 3-4 in the optimistic scenario where systematics are fully under control. We caution that achieving these forecasts will likely require a full analysis of higher-order biasing, photometric redshift uncertainties, and stringent control of other systematic limitations, which are outside the scope of this work, whose primary purpose is to elucidate the physical origin of the constraints.

**Key words:** cosmology: dark energy – cosmic background radiation – large-scale structure of Universe

## 1 INTRODUCTION

Future surveys of the Cosmic Microwave Background (CMB) in intensity and polarization will produce high signal-to-noise ratio (SNR) CMB lensing maps over a large fraction of the sky. The survey conducted from the Atacama Plateau in Chile by CMB-S4 (Abazajian et al. 2016) will have significant spatial overlap with the deep and wide photometric galaxy catalogs to come from the Vera C. Rubin Observatory, an optical facility located at Cerro Pachón, also in Chile (Abell et al. 2009). For the first ten years of operation, the Rubin Observatory will perform the Rubin Observatory Legacy Survey of Space and Time (LSST).

In this paper we investigate physical origin of the constraints on the dark energy equation of state (EoS) parameter  $w$  that can be obtained by cross-correlating redshift-binned galaxy maps and a high SNR CMB lensing map. We choose to not include the forecasts of galaxy weak lensing (WL), in order to find out what can be achieved without

WL and to create a complementary probe to those which do include WL. We have previously explored the physical origin neutrino mass constraints in a very similar setup in the companion paper (Yu et al. 2018).

Varying the EoS parameter of dark energy affects both the expansion rate of the Universe and the growth of large-scale structure (LSS), which impacts both the amplitude of the matter power spectrum and the angular position of the Baryon Acoustic Oscillation (BAO) features within it. The distribution of galaxies within a narrow redshift bin traces the distribution of matter at that redshift, and therefore its map and power spectrum contain information about expansion and growth in the same redshift range. On the other hand, the lensing of the CMB traces the distribution of matter over a wide range of redshifts, combined into a single map and power spectrum. Galaxy surveys measure the luminous matter, while lensing is sensitive to the underlying matter distribution, so we expect the cross-correlation between galaxies and lensing to provide a measurement of the relationship between luminous and dark matter (Abazajian et al. 2016), crucially breaking the intrinsic degeneracy between the amplitude of fluctuations and galaxy bias. Our goal is to describe the benefit of

\* E-mail: bhyu@berkeley.edu (BY)

† E-mail: sferraro@lbl.gov (SF)

combining these two sources of information, particularly in how they together can inform us on the dark energy EoS parameter.

The cross-correlation of redshift-binned maps of galaxy number densities with CMB lensing is very useful due to the different ways in which galaxy clustering and CMB lensing are dependent on the galaxy bias. We use the standard definition of the linear galaxy bias as the ratio of the overabundance of galaxies to the overdensity of mass,  $b(z) = \delta_g(\mathbf{r})/\delta(\mathbf{r})$ ;  $\delta_g(\mathbf{r}) = (n(\mathbf{r}) - \bar{n})/\bar{n}$ , where  $n(\mathbf{r})$  is the density of galaxies at location  $\mathbf{r}$  and  $\bar{n}$  is its spatial average, and  $\delta(\mathbf{r}) = (\rho(\mathbf{r}) - \bar{\rho})/\bar{\rho}$ , where  $\rho(\mathbf{r})$  is the mass density at a location  $\mathbf{r}$  and  $\bar{\rho}$  is its spatial average. We can then determine such linear and scale-independent bias, to within noise limitations, as the ratio between angular power spectra,  $b_i \approx C_l^{g_i g_i} / C_l^{K_i g_i}$ , where  $i$  runs over tomographic redshift bins. With improved constraints on galaxy bias at various redshifts, we can break the degeneracy between galaxy bias and the amplitude of the matter power spectrum  $P(k, z)$ , thereby better constraining the cosmological model parameters (Pen 2004; Schmittfull & Seljak 2017).

Giannantonio et al. (2016) used the high depth and density of the DES survey to construct maps of galaxy number density in several photometric redshift bins. They then cross-correlated these maps with a CMB lensing map inferred from *Planck* and SPT data in order to determine both the galaxy bias and the CMB lensing amplitude, in a process they called ‘‘CMB lensing tomography’’ (see for example Sherwin et al. (2012); Bleem et al. (2012a); Planck Collaboration et al. (2014) for early work and Planck Collaboration et al. (2018); Omori et al. (2018); Krolewski et al. (2020); Marques & Bernui (2020); Darwish et al. (2021); Hang et al. (2021); Kitanidis & White (2021); Krolewski et al. (2021b); Garca-Garca et al. (2021); Chen et al. (2021) for more recent analyses).

CMB lensing tomography provides us with a means, complementary to tomographic cosmic shear, of reconstructing the mass distribution across the sky in coarse slices in redshift. Here we study the role, in reaching constraints on dark energy parameters, of not just the amplitude as a function of redshift, but also the shape of the matter power spectrum, and the distance-redshift relation that influences observables that are all seen in projection.

In this paper we focus on the constraints on dark energy that can come from the CMB lensing tomography enabled by CMB-S4 lensing maps and LSST galaxy clustering. Current SNRs for the best-measured modes in CMB lensing maps are quite modest. The *Planck* lensing map (Ade et al. 2016), has a SNR per mode (on spherical harmonic modes with multipole moment  $l$ ) approximately equal to 1 for  $l \approx 50$ , and lower everywhere else. From CMB-S4 we expect SNRs of greater than unity for all modes with  $l \lesssim 1000$  and as large as  $\approx 40$  for the best-measured modes. This increase in CMB lensing precision, together with LSST galaxy clustering, opens up the possibility of measuring the amplitude of structure to a high precision over a range of redshifts (Abazajian et al. 2016).

The roles of ‘‘geometry’’ (the distance-redshift relation) and ‘‘growth’’ (the amplitude of the matter power spectrum as a function of time) have been well-studied in the case of tomographic cosmic shear (Abazajian & Dodelson 2003; Simpson & Bridle 2005; Zhang et al. 2005; Knox et al. 2006; Zhan & Knox 2006; Zhan et al. 2008; Matilla et al. 2017; Zhan & Tyson 2018). Although often described as a probe of growth, distinguishing it from purely geometric probes such as the use of SNeIa as standard candles, these studies clarify that geometry is just as important as growth, if not more so, for constraints on dark energy parameters.

Several forecasts have been done for cosmological parameter sets which include  $\Sigma m_\nu$  and  $w$ , through several combinations of observables that include WL, high-SNR CMB lensing, and galaxy cluster-

ing. Early forecasts which included either WL or CMB lensing either did not include galaxy clustering (Kaplinghat et al. 2003; Hannestad et al. 2006; Namikawa et al. 2010; Wu et al. 2014), or did not include the cross-correlation between CMB lensing and galaxy clustering (Santos et al. 2013; Krause & Eifler 2017; Eifler et al. 2021). More recently, studies have gone to the opposite extreme. That is, recent studies have included the cross correlation between CMB lensing and galaxy clustering, as part of a robust and inclusive forecast that also includes the cross-correlations between cosmic shear and galaxy clustering, and between cosmic shear and CMB lensing. However, these studies did not attempt to forecast the benefits of the CMB lensing - galaxy clustering cross-correlation, without also including WL cross-correlations (Joudaki & Kaplinghat 2012; Mishra-Sharma et al. 2018; Schaan et al. 2017).

Two studies which we follow very closely are those of Schmittfull & Seljak (2017) and the companion to this paper, Yu et al. (2018), in which we presented forecasts of  $\Sigma m_\nu$  that include CMB-S4 lensing, LSST galaxy clustering, and their cross-correlation, but did not forecast the dark energy figure of merit. The forecast of Schmittfull & Seljak (2017) includes a forecast of  $\sigma_8$ , the linear theory RMS of the mass distribution on scales of 8 Mpc/h, which effectively serves as a proxy for the amplitude of the matter power spectrum.

Schaan et al. (2020) considered the impact of photometric redshift uncertainties and the potential for self-calibration in a setup similar to ours. That work shows that the fraction of photometric redshift outliers can be constrained by the data itself, and it considers the effect of dynamical Dark Energy and neutrinos, similar to this forecast. Fang et al. (2021) explores constraints from cosmic shear, clustering and CMB lensing, including the effect of baryons and photo- $z$  outliers. However, the physical origin of the constraints on Dark Energy, the main goal of the present paper, was not explored in these works.

The remainder of our paper is organized as follows: In Section 2, we present our cosmological model space and assumptions about observables and noise. Consistent with our focus on understanding the physics that leads to the forecasted constraints, our modeling of the data is quite simple, and in particular does not include sources of systematic error. In Section 3 we describe our forecasting formalism and in Sections 4 and 5 we present and discuss our results. Note that we discuss the physical origin of dark energy constraints in Section 2.3 and 4.1.

## 2 MODEL AND ASSUMPTIONS

In the companion paper (Yu et al. 2018) we assume the  $\Lambda$ CDM model extended to include massive neutrinos, and here we further extend it to include time-varying dark energy. The cross-correlations are computed in spherical harmonic space and take the form of angular power spectra.

We assume a fiducial model with the following parameters:  $\Omega_b h^2 = 0.02226$ ,  $\Omega_c h^2 = 0.1193$ ,  $\tau = 0.063$ ,  $A_s = 2.130 \times 10^{-9}$ ,  $n_s = 0.9653$ ,  $\theta_{MC} = 1.04087 \times 10^{-2}$ , and  $\Sigma m_\nu = 0.06$  eV. The neutrinos in this model are relativistic in the early universe and slow down as the universe expands, becoming non-relativistic at late times. We add time-varying dark energy by considering the dark energy equation of state parameter  $w$  to follow the common parameterization (Chevallier & Polarski 2001; Linder 2003)  $w(a) = w_0 + (1 - a)w_a$ , where  $a$  is the scale factor of the expansion of the universe normalized such that  $a = 1$  today, while noting that different parameterizations are possible (Jassal et al. 2005; Efstathiou 1999; Barboza & Alcaniz 2008; Colgain et al. 2021). The fiducial values that we use are

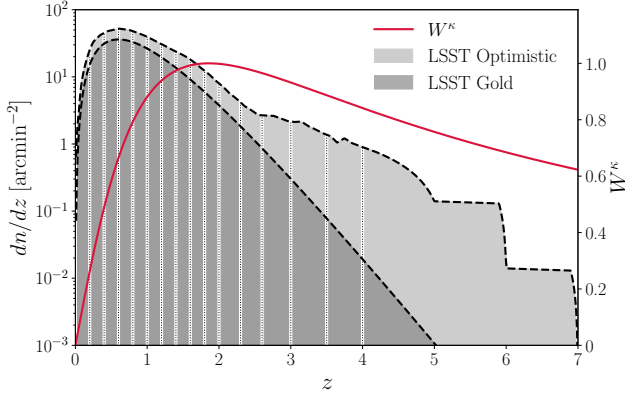


**Figure 1.** The redshift distribution of the CMB lensing convergence kernel (red curve, normalized to a unit maximum) and LSST galaxy samples, both Optimistic (light gray) and Gold (dark gray). We assume 16 tomographic redshift bins in the range  $0 < z < 7$ , and indicate bin boundaries with vertical lines.

$w_0 = -1$ ,  $w_a = 0$ . We also include one galaxy bias parameter for each galaxy bin, as described in section 2.1.

## 2.1 Galaxy Binning

Following Yu et al. (2018), we employ two different assumptions for LSST galaxy redshift distributions in our analysis, as shown in figure 1. The first redshift distribution is the  $i < 25$  Gold sample (Abell et al. 2009), which takes the analytic form  $dN(z)/dz \propto (1/2z_0)(z/z_0)^2 e^{-z/z_0}$ , with  $z_0 = 0.3$  and a corresponding galaxy solid angle number density of  $\bar{n} = 40 \text{ arcmin}^{-2}$ , and is hereafter referred to as the “LSST Gold” sample. The second distribution, which we refer to as the “LSST Optimistic”, assumes a fainter observable magnitude limit of  $i < 27$  with  $S/N > 5$  in the  $i$  band and includes Lyman break galaxies from redshift dropouts, and this results in the increase the number density of observable galaxies to  $\bar{n} = 66 \text{ arcmin}^{-2}$  (Schmittfull & Seljak 2017). This large number density may not be overly optimistic for our purposes as we do not rely on galaxy shape measurements, but just galaxy locations.

We divide LSST galaxy redshift distributions into 16 non-overlapping tomographic bins with the bin edges of  $z = [0, 0.2, 0.4, 0.6, 0.8, 1, 1.2, 1.4, 1.6, 1.8, 2, 2.3, 2.6, 3, 3.5, 4, 7]$ . Defining redshift bins with perfectly sharp edges in an actual galaxy survey, however, is not currently achievable, as the high number of galaxies can only have their redshifts determined photometrically, with an associated photometric redshift error. Thus our forecasts describe the ideal case in which the photometric redshift (“photo- $z$ ”) error has been completely eliminated. This is a conceptually simpler case than one in which the redshift bins are more realistic and contain the photo- $z$  error, and we leave the forecasting that includes such error to a future study.

Likewise, our idealized treatment neglects a number of effects that should be included in more realistic forecasts. These include effects of galactic dust, photometric redshift errors (e.g. Hildebrandt et al. (2016); Schaun et al. (2020)), galaxy-galaxy blending (Hartlap et al. 2011), and magnification-induced correlations across redshift bins (e.g. González-Nuevo et al. (2017)). Also, we neglect any non-Gaussian corrections to the covariance matrix (Takada & Hu 2013; Krause & Eifler 2017). As stated above, we find that this simplified setting is helpful to elucidate the physical origin of the constraints,

and we don’t expect our conclusions to change when considering a more realistic forecast.

We use galaxies as tracers of matter and assume a single galaxy population. We use a linear galaxy bias model, which Crocce et al. (2015) show to be valid (in the Dark Energy Survey) at least on the scales where the linear growth of structure is a sufficiently accurate approximation. Similarly, we’ll restrict our analysis to large scales (defined below), and use the linear matter power spectrum. More sophisticated modeling of non-linearities in matter and bias will be required in a more realistic analysis (see for example Modi et al. (2017); Krolewski et al. (2021a); Kitaniid & White (2021); Pandey et al. (2021)). Following Schmittfull & Seljak (2017), we use  $b(z) \propto 1 + z$  as our fiducial bias evolution. The exact value of this function should not be important, though higher biases would lead to higher-amplitude galaxy power spectra without increasing the shot noise, and therefore tighter parameter constraints.

For each redshift bin, we define a bias parameter calculated as a weighted average of this galaxy bias function over the redshift range of the bin:

$$b_i = \frac{1}{\left[ \int \frac{dN_i(z')}{dz'} dz' \right]} \int \frac{dN_i(z)}{dz} b_i(z) dz, \quad (1)$$

where  $b_i(z) = B_i b(z)$ .  $B_i$  is effectively an amplitude of the bin bias, and  $b(z)$  is the redshift dependent galaxy bias function. The  $B_i$  parameters are the ones that we use in our Fisher forecasting, with fiducial values of  $B_{i, fid} = 1$ . Similarly,  $b_{i, fid} = b_i(B_{i, fid})$ , which leads to  $\sigma(B_i) = \sigma(b_i)/b_{i, fid}$  in the Fisher results.

## 2.2 Theoretical Power Spectra

With the CMB lensing convergence  $\kappa$  and a tomographic set of galaxy distribution map, we compute the following 2-point angular power spectra:  $C_l^{\kappa\kappa}$ ,  $C_l^{\kappa g_i}$ , and  $C_l^{g_i g_i}$ , where  $g_i$  is the galaxy density field in the  $i$ th tomographic redshift bin.

The CMB lensing convergence in direction  $\hat{n}$  can be calculated as a line-of-sight integral over the fractional matter over-density  $\delta(\mathbf{r}, z)$  at the comoving position  $\mathbf{r}$  and redshift  $z$ :

$$\kappa(\hat{n}) = \int d\chi W^\kappa(\chi) \delta(\chi \hat{n}, z(\chi)), \quad (2)$$

where  $\chi$  is the the comoving distance, and the lensing distance kernel is (Cooray & Hu 2000; Song et al. 2003; Bleem et al. 2012b):

$$W^\kappa(\chi) = \frac{3}{2} \Omega_m H_0^2 \frac{\chi}{a(\chi)} \frac{\chi_{\text{CMB}} - \chi}{\chi_{\text{CMB}}}, \quad (3)$$

where  $\Omega_m$  is the matter fraction at the current time,  $H_0$  is the current value of the Hubble parameter,  $a(\chi)$  is the scale factor at comoving distance  $\chi$ , and  $\chi_{\text{CMB}}$  is the comoving distance of the CMB’s surface of last scattering.

For the galaxy density field in the  $i$ th bin, we can also calculate the following line-of-sight integral:

$$g_i(\hat{n}) = \int d\chi W^{g_i}(\chi) \delta(\chi \hat{n}, z(\chi)), \quad (4)$$

where the galaxy distance kernel is (Bleem et al. 2012b):

$$W^{g_i}(\chi) = \frac{1}{\left[ \int dz' \frac{dN_i(z')}{dz'} \right]} \frac{dz}{d\chi} \frac{dN_i(z)}{dz} b_i(\chi). \quad (5)$$

**Table 1.**  $l_{\max}$  values corresponding to two  $k_{\max}$  limits, 0.1 and  $0.2 h\text{Mpc}^{-1}$ , for the left edge of each tomographic redshift bin. ( $l_{\max}$  is therefore set to be zero for the first bin.) We assume  $l_{\min} = 30$  to account for the expected difficulty of attaining low-noise data on large angular scales.

$k_{\max} \setminus \text{bin}$	1	2	3	4	5	6	7	8
0.1	0	57	108	153	193	229	261	289
0.2	0	114	216	307	387	459	522	579
$k_{\max} \setminus \text{bin}$	9	10	11	12	13	14	15	16
0.1	315	338	358	386	411	439	469	495
0.2	630	676	717	773	822	879	939	991

Note that we neglect the magnification bias.

Using the Limber approximation (Limber 1953; Kaiser 1992), we model the angular power spectrum as:

$$C_l^{\alpha\beta} = \int dz \frac{d\chi}{dz} \frac{1}{\chi^2} W^\alpha(\chi) W^\beta(\chi) P_{\delta_\alpha \delta_\beta} \left( \frac{l+1/2}{\chi}, z(\chi) \right) \quad (6)$$

where  $\alpha, \beta \in (\kappa, g_1, \dots, g_N)$ , and  $P(k, z)$  is the matter power spectrum at wavenumber  $k$  and redshift  $z$ . We use the CDM-baryon density contrast  $\delta_{cb}$  for galaxy clustering and the total matter density contrast  $\delta_{cb\nu}$  (which includes neutrinos) for lensing.

We use the publicly available CAMB code (<https://camb.info/2021>; Lewis et al. 2000) and its Python wrapper (<http://camb.readthedocs.io/en/latest/> 2021) in order to calculate  $P(k, z)$ , as well as the unlensed primary CMB power spectra  $C_l^{TT}$ ,  $C_l^{TE}$ , and  $C_l^{EE}$ . For such calculations, we assume the normal hierarchy, in which the third neutrino mass eigenstate  $\nu_3$  is heavier than the other two eigenstates. We use the fluid dark energy model implemented in the python wrapper of CAMB, available since its major update in version 1.0.

As in Yu et al. (2018), we impose the limit on the maximum wavenumber to be included in our analysis (see Table 1 for the corresponding  $l_{\max}$  values of each redshift bin) so that perturbations can be assumed to remain in the linear regime, and therefore uncertainties due to non-linear modeling have negligible effects on our forecasts. All forecasts presented in this work assume the linear matter power spectrum, as we find that the effects of adding non-linear corrections from HALOFIT to the power spectrum are only negligible with  $k_{\max} = 0.1$  or  $0.2 h\text{Mpc}^{-1}$  imposed.

### 2.3 Separating Impacts of Distance, Growth, and Shape

The EoS parameter of dark energy affects both the cosmic distance scale and the growth factor. The relative importance of these two effects on constraining the EoS parameter has been discussed for WL by several groups (Abazajian & Dodelson 2003; Simpson & Bridle 2005; Zhang et al. 2005; Knox et al. 2006; Zhan & Knox 2006; Zhan et al. 2008; Matilla et al. 2017), using various methods. As was shown by Simpson & Bridle (2005) and by Matilla et al. (2017), there is a partial cancellation of the geometry and growth effects for WL observables when  $w$  is varied.

In Figure 2 and 3, we vary  $w_0$  while keeping the angular size of the sound horizon  $\theta_{\text{MC}}$ ,  $\omega_b$ , and  $\omega_m$  fixed in order to make minimal changes to primary CMB power spectra. In this scenario, if we increase  $w$  from its fiducial value, the dark energy density decreases with time. In order to keep  $\theta_{\text{MC}}$  fixed, and therefore the angular-diameter distance to last-scattering fixed, we increase the dark energy density at high redshifts. The result is that, compared to the fiducial model, with  $w_0$  increased  $H(z)$  is decreased at  $z \lesssim 0.9$

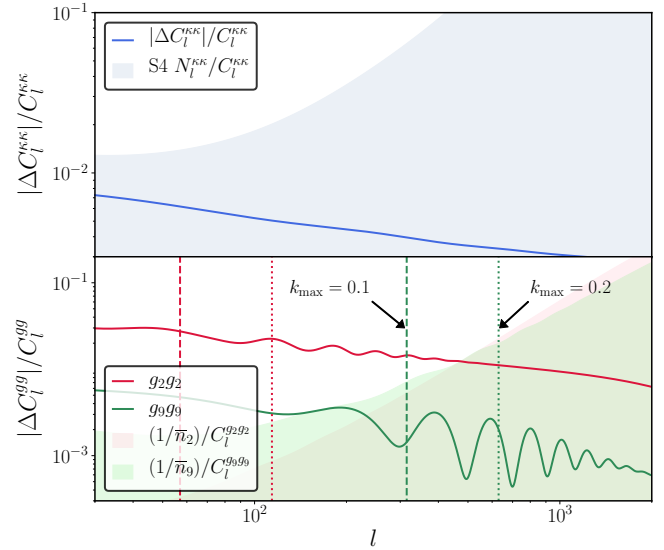


**Figure 2.** Fractional change of the auto-power spectra  $C_l^{KK}$  and  $C_l^{gg}$  with respect to  $\Delta w_0$ :  $|\Delta C_l|/C_l = \frac{1}{C_l} |\Delta w_0 \times \partial C_l / \partial w_0|$ , where  $\Delta w_0 = 0.05$ .  $\theta_{\text{MC}}$  is held fixed. *Top*: Comparison between the S4 lensing reconstruction noise (blue shaded region) and the changes in the CMB lensing auto-power spectrum with respect to  $\Delta w_0$  (blue curve). *Bottom*: The galaxy shot noise and the changes in the galaxy auto-power spectra with respect to  $w_0$ , in the 2nd (red) and 9th (green) tomographic redshift bin. Also shown are vertical lines indicating the  $l_{\max}$  values for each redshift bin, corresponding to the two  $k_{\max}$  values indicated in Table 1.

and gently increased at  $z \gtrsim 0.9$ , asymptoting to zero increase deep in the dark-matter-dominated regime. One result is that the distances to all redshifts at  $z \lesssim 1100$  are increased, asymptoting to zero change deep in the dark-matter dominated regime. Another is that at  $z \gtrsim 0.9$ , growth is slowed down. The impact on the growth reverses when  $H(z)$  starts to become less than in the fiducial model at  $z \approx 0.9$ . Figure 3 indeed shows  $\Delta P(k) < 0$  for  $\Delta w > 0$ , with more power suppression at  $z \approx 0.5$  than for any of the other redshift choices shown in the figure. On the other hand, increasing  $w$  leads to  $D(z) > 0$  at all redshifts (asymptoting to zero at high redshift), thereby increasing the angular power spectrum  $C_l$ . We find that these two effects partly cancel each other leading to weaker cosmological constraints than if growth and distance were measured separately, as we shall see below. Note that in Figure 3,  $P(k)$  is suppressed at all redshifts, and therefore there is partial cancellation in all redshift bins.

One way of comparing the relative importance of distance and growth on constraining  $w$  in a Fisher forecast is to split  $w$  into two components:  $w_d$ , which only affects the distance, and  $w_g$ , which affects the growth only. Previous work has used this parametrization to distinguish between the two effects and systematic errors (Zhang et al. 2005), or to investigate which has more constraining power (Simpson & Bridle 2005; Zhan et al. 2008). Zhan & Knox (2006) extends this idea of splitting the parameter  $w$  to examine constraints on  $(w_0, w_d)$  for distance-only, growth-only, and full (growth+distance) cases, finding that the growth-only case has the least constraining power; with other cosmological parameters marginalized, the full case has the most constraining power, while fixing them make the distance-only case more powerful.

We instead apply a similar procedure to investigate the relative importance of distance and growth in our forecasts, but we take an additional step of separating the growth effect further into two sepa-

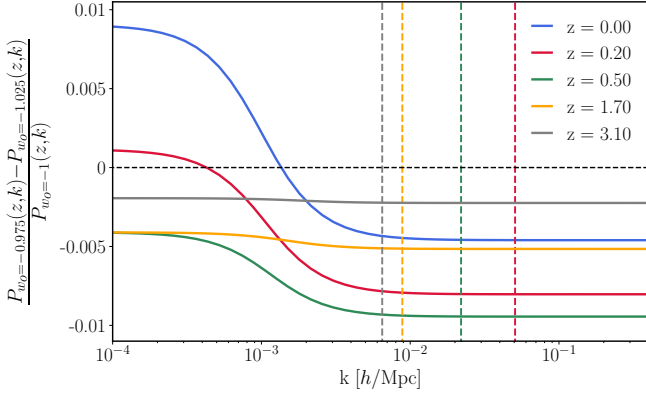


**Figure 3.** Fractional change of the matter power spectrum  $P(z, k)$  with respect to  $w_0$  ( $\Delta w_0 = 0.05$ ),  $\Delta P(z, k)/P(z, k)$ , for five different redshifts within the range of our analysis.  $\theta_{MC}$  is held fixed. To preserve the distance to the last scattering surface, the vertical dashed lines correspond to the low- $l$  cutoff ( $l_{\min} = 30$ ) used in the Fisher forecasts, de-projected to the redshifts (from the right) 0.2, 0.5, 1.7, and 3.1. With the resulting  $k$ -limits, we remove dark energy perturbations on large scales from the analysis, thereby making the power spectrum shape effects negligible.

rate components: the growth of amplitude of the power spectrum and the change in the shape of the power spectrum due to growth. The reason for such decomposition is the degeneracy between the power spectrum amplitude and the galaxy bias, and we break this degeneracy by incorporating observables which have different dependencies on galaxy bias<sup>1</sup>.

Figure 3 shows the fractional change in  $P(z, k)$  due with respect to  $\Delta w_0$  for five different values of redshift. We only show the plots for  $w_0$ , but  $w_a$  derivatives are very similar in appearance. The absence of scale-invariance seen in this figure is a generic effect associated with  $w \neq -1$  dark energy models, as pointed out by e.g. [Bean & Doré \(2004\)](#) and [Unnikrishnan et al. \(2014\)](#), who showed that dark energy perturbations appear on very large scales, depend in particular on the sound speed, and are model dependent.

At first glance, Figure 3 looks as if ignoring the shape of  $w$  derivatives is effectively flattening the large low- $k$  features in the derivatives. However, these features occur on scales much larger than the maximum angular scale we include in the analysis. Due to the possibility of large-scale systematics, we also impose a low- $l$  cutoff of  $l_{\min} = 30$  for each redshift bin. We check that with the resulting  $k$ -limits, shown as vertical lines in Figure 3, we remove large perturbative features from the  $w$  derivatives. The portion of the power spectrum greater than these cut-off points differs from the shape-less version (identical to the value at  $k = 0.01 h\text{Mpc}^{-1}$ ) by only several hundredths of a percent. Due to the smallness of this feature, we can safely neglect it.

When we calculate the partial derivatives of the observables with respect to the  $w_0, w_a$  parameters,  $P(k, z)$  in each tomographic redshift bin is fixed to the value of  $P(k, z_{\text{med}})$ , where  $z_{\text{med}}$  is the median redshift of each bin, to remove  $w(a)$ -dependent variations of the power spectrum across the width of each bin. Such variations, degenerate with the evolution of bias across the bin, can make our results artificially sensitive to those changes, especially given that

<sup>1</sup> CMB lensing has no galaxy bias dependence whereas galaxy observations do, which allows the combination of the various observables  $C_l^{g_i g_i}, C_l^{K g_i},$  and  $C_l^{K K}$  to distinguish a change in amplitude from the galaxy bias.

we fix the bias evolution within each bin. We find that overlooking such procedure can lead to artificially rosy forecasts, increasing the constraining power by tens of percent.

### 3 FISHER FORECASTING

We use the Fisher information matrix formalism to forecast constraints on the cosmological parameters of interest ([Tegmark et al. 1997](#); [Bassett et al. 2011](#)).

#### 3.1 Observables

We forecast the constraining power of cross-correlating CMB-S4 lensing with the galaxy clustering tomography observations of Rubin Observatory LSST (similar to [Giannantonio et al. \(2016\)](#)), and our observables are auto- ( $C_l^{K K}$  and  $C_l^{g_i g_i}$ ) and cross-spectra ( $C_l^{K g_i}$ ) from Section 2.2. We do not include  $C_l^{g_i g_j}$ , cross-spectra of galaxy tomographic bins, nor do we include the cross-spectrum  $C_l^{T K}$ , which would be nonzero at low  $l$  due to the gravitational Integrated Sachs-Wolfe (ISW) effect.

For CMB lensing, we assume a CMB-S4 experiment with the telescope beam of Full-Width-Half-Maximum (FWHM) of  $1'$  and a white noise level of  $1\mu K'$  for temperature and  $1.4\mu K'$  for polarization. We assume  $f_{\text{sky}} = 0.4$  and set the noise levels  $N_l^{TT}, N_l^{EE}$  in the primary CMB as a Gaussian noise as:

$$N_l^{XX} = s^2 \exp\left(l(l+1) \frac{\theta_{\text{FWHM}}^2}{8 \log 2}\right), \quad (7)$$

where  $XX$  stands for  $TT$  or  $EE$ ,  $s$  is the total intensity of instrumental noise in  $\mu K\text{rad}$ , and  $\theta_{\text{FWHM}}^2$  is the FWHM of the beam in radians ([Wu et al. 2014](#)). For the CMB lensing reconstruction noise, we use the EB quadratic estimator method described in [Hu & Okamoto \(2002\)](#), implemented by the QUICKLENS (<https://github.com/dhanson/quicklens> 2017) software package. Following [Schmittfull & Seljak \(2017\)](#), we rescale the EB noise to approximately match the expected improvement from iterative lens reconstruction for CMB-S4 ([Hirata & Seljak 2003](#); [Smith et al. 2012](#)).

For the LSST, we assume that the survey covers an area on the sky of  $18,000 \text{ deg}^2$ , corresponding to  $\approx 40\%$  of the sky, and that it fully overlaps with CMB-S4. The shot noise associated with the galaxy redshift distributions is  $1/\bar{n}_i$ , where  $\bar{n}_i$  is the galaxy number density per redshift bin, calculated per bin from the ratio of the integrated area of  $dN_i/dz$  to that of the total  $dN(z)/dz$  multiplied by the overall galaxy density  $\bar{n}$ .

#### 3.2 Fisher Matrices

Assuming our observables from Section 3.1 are the power spectra of Gaussian random fields, we can compute the covariance matrix as:

$$\text{Cov}(C_l^{\mu_1 \nu_1}, C_l^{\mu_2 \nu_2}) = \frac{\delta_{ll'}}{(2l+1)f_{\text{sky}}} \left( C_l^{\mu_1 \mu_2} C_l^{\nu_1 \nu_2} + C_l^{\mu_1 \nu_2} C_l^{\nu_1 \mu_2} \right), \quad (8)$$

where  $(\mu_1, \mu_2, \nu_1, \nu_2) \in \{K, g_1, \dots, g_N\}$ . We assume that each  $C_l$  contains both signal and noise.

Then, the Fisher matrix is given by:

$$F_{ij} = \sum_{\mu_1, \nu_1} \sum_{\mu_2, \nu_2} \frac{\partial C_l^{\mu_1 \nu_1}}{\partial \theta_i} \left[ \text{Cov}(C_l^{\mu_1 \nu_1}, C_l^{\mu_2 \nu_2}) \right]^{-1} \frac{\partial C_l^{\mu_2 \nu_2}}{\partial \theta_j}, \quad (9)$$

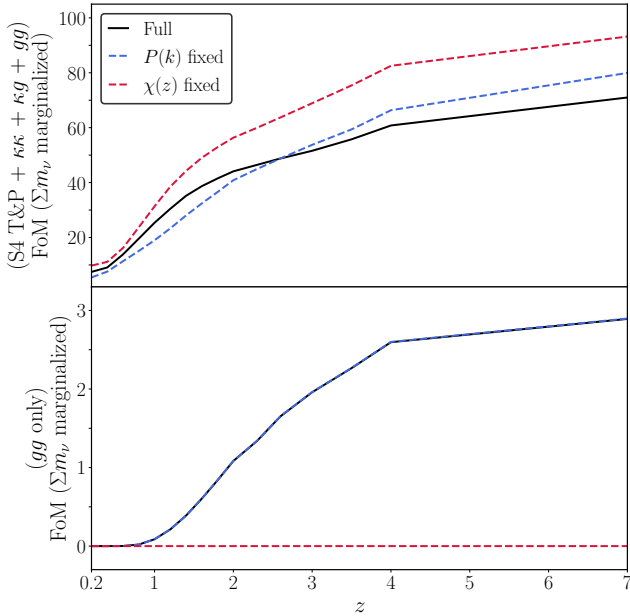


**Figure 4.** Forecasted DETF Figure of Merit, defined as  $[\sigma(w_a)\sigma(w_p)]^{-1}$ , with changes to either growth (blue) or geometry (red) disregarded. We also include the results with the “full” Fisher matrix (black), where we apply no restrictions (all effects included), for comparison. *Top:* 1/EP from the combination of S4 primordial CMB, S4 lensing, and LSST clustering (using Optimistic  $dN(z)/dz$  with  $k_{\max} = 0.2h\text{Mpc}^{-1}$ ). We observe the partial cancellation between growth and geometry. *Bottom:* Only with LSST galaxies, ignoring changes to geometry (by fixing  $\chi(z)$ ) makes the constraining power negligibly small.

where  $\vec{\theta}$  is a set of cosmological model parameters from Section 2. We can combine the Fisher matrix in equation 9 with external datasets, such as the primordial CMB and BAO Fisher matrices, if needed and then invert the resulting matrix to determine the marginalized constraints on the parameters of our interest.

## 4 FORECAST RESULTS

We frame our  $w_0$ ,  $w_a$  forecasts in terms of an Error Product (EP), which is inversely proportional to the Dark Energy Task Force (DETF) Figure of Merit (FoM) (Albrecht et al. 2006), defined as the inverse of the area of an error ellipse in the  $w_0$ ,  $w_a$  plane. Hence, a higher FoM corresponds to a smaller error. The EP is a simpler alternative to the FoM, defined as  $\sigma(w_a) \times \sigma(w_p)$ , where  $w_p = w(a_p)$ , and  $a_p$  is the scale factor at which the uncertainty in  $w$  is the least (Zhan 2006; Abell et al. 2009). In this work, we assume that  $\text{FoM} \equiv 1/\text{EP}$ .

Table 2 and Figure 6 present constraints on the the neutrino mass dark energy equation of state, marginalized over  $\Lambda\text{CDM}$  parameters and linear galaxy bias amplitudes in all bins, for different experiment configurations and  $k_{\max}$  limits. We find that the relative merit of cross-correlating CMB lensing with galaxy clustering is huge; with  $k_{\max} = 0.2h\text{Mpc}^{-1}$ , combining the galaxy clustering from the LSST Optimistic sample and CMB-S4 lensing can achieve the FoM (1/EP) of 71. We assume that the primordial CMB information is included in all forecasts.

### 4.1 Growth or Geometry?

To investigate how sensitive our forecasts are to the distance-redshift relation (geometry) and the amplitude of the matter power spectrum as a function of redshift (growth), we make the following different types of forecasts: “ $P(k)$  fixed”, for which we do not allow the power spectrum to change as  $w$  changes, “ $\chi(z)$  fixed”, for which we do not let the distance-redshift relationship change as  $w$  changes, and “Full” for which we apply no restrictions.

Figure 4 shows the result of FoM forecasts for all three cases, using the LSST Optimistic  $dN(z)/dz$  with  $k_{\max} = 0.2h\text{Mpc}^{-1}$ . We present FoM values as functions of redshift: at each redshift, only bins at and below that redshift are included, and FoM increases as we extend the redshift lever arm and thereby include more galaxies, as expected.

The top panel of Figure 4 shows the forecasts of CMB lensing and LSST clustering combined. We note that both geometry and growth play a significant role, as can be seen by comparing the red and blue curves; the “Full” Fisher matrix (black curve), which include all of the effects, appears to have less constraining power than either geometry or growth, suggesting that there is a partial cancellation at play. A similar cancellation was noted for WL observables in Simpson & Bridle (2005); Matilla et al. (2017) and we find that this applies to clustering measurements as well. In short, we note that the partial cancellation between growth and geometry effects that has been noticed before also appears in our S4 lensing + LSST forecasts.

We also find that inclusion of CMB lensing increases the FoM by a factor of 3-4 (over the S4 primary CMB + gg result not shown in Figure 4), suggesting that cross-correlations between CMB lensing and galaxy clustering provide a very competitive dark energy probe. The bottom panel shows that with only LSST galaxies, “ $\chi(z)$  fixed” case has a negligibly small constraining power, as we cannot gain any dark energy information if the distance-redshift relation is fixed, and the amplitude of power spectrum is degenerate with bias.

### 4.2 Comparisons with Galaxy Weak Lensing Forecasts

Zhan (2006) presents LSST Cosmic Shear + *Planck* forecasts of the EP  $[\sigma(w_a)\sigma(w_p)]$ , for various levels of photometric redshift error, on which the EP depends. Our forecasts assume zero uncertainty in the redshifts of the observed galaxies. Our redshift bin widths are  $\Delta z = 0.2$  for the lowest redshift bins up until  $z = 2$ , then  $\Delta z = 0.3-0.5$  out to redshift  $z = 4$ , and the final bin width of  $\Delta z = 3.0$  from  $z = 4$  to  $z = 7$ . To reduce the sensitivity to photo- $z$  errors, we make the bin widths wider than the expected rms scatter in photo- $z$  errors, but we acknowledge that the effects of photo- $z$  errors are not entirely eliminated. We leave an analysis of quantifying such impacts to future work. Zhan (2006) provides the EP as a function of  $\sigma_z/(1+z)$ , where  $\sigma_z$  is the rms photometric redshift error. For simplicity, we compare against the EP corresponding to two specific values of redshift error:  $\text{EP} \approx 0.011$  for  $\sigma_z/(1+z) = 0$  and  $\text{EP} \approx 0.015$  for  $\sigma_z/(1+z) = 0.05$ , and these forecasts appear as black horizontal lines in the middle panel of Figure 5, labeled as “Planck T&P + LSST Cosmic Shear.” We find that our results are at a similar level to these cosmic shear forecasts. We also note that the middle and bottom panels of Figure 5 provides the FoM forecasts with fixed  $\Sigma m_\nu$  to make a fair comparison to the forecasts in Zhan (2006).

However, the forecasts in Zhan (2006) assume slightly different choices for the survey characteristics. For the LSST specifications, Zhan (2006) assumes  $f_{sky} = 0.48$  and uses a full-survey galaxy number density of  $\bar{n} = 50$  galaxies/arcmin<sup>2</sup>, while we use  $f_{sky} = 0.4$  and  $\bar{n} = 40$  galaxies/arcmin<sup>2</sup>. Moreover, Zhan (2006) uses a fiducial

(+ S4/Planck T&P)	$\Lambda$ CDM + $m_\nu$ free		+ $w_0, w_a$ free									
	$\sigma(\Sigma m_\nu)$ [meV]		$\sigma(w_0)$		$\sigma(w_a)$		$\sigma(w_p)$		1/EP		$\sigma(\Sigma m_\nu)$	
S4Lens	69		0.25		0.95		0.14		7.5		83	
	$k_{\max} = 0.2$	0.1	0.2	0.1	0.2	0.1	0.2	0.1	0.2	0.1	0.2	0.1
S4Lens + LSST Gold	36	50	0.12	0.18	0.37	0.50	0.050	0.085	54	23	55	61
+ DESI BAO	22	23	0.093	0.11	0.28	0.31	0.026	0.029	138	111	39	41
S4Lens + LSST Optimistic	31	41	0.10	0.15	0.33	0.46	0.042	0.077	71	28	48	54
+ DESI BAO	21	22	0.085	0.11	0.26	0.31	0.024	0.028	159	117	37	40

**Table 2.** Forecasts of the neutrino mass and dark energy constraints, for different experiment configurations and  $k_{\max}$  limits. The first two columns assume the dark energy parameters are held fixed, while marginalizing over six  $\Lambda$ CDM parameters and linear bias amplitudes in tomographic bins, and the rest of the columns include  $w_0$  and  $w_a$  as free parameters.

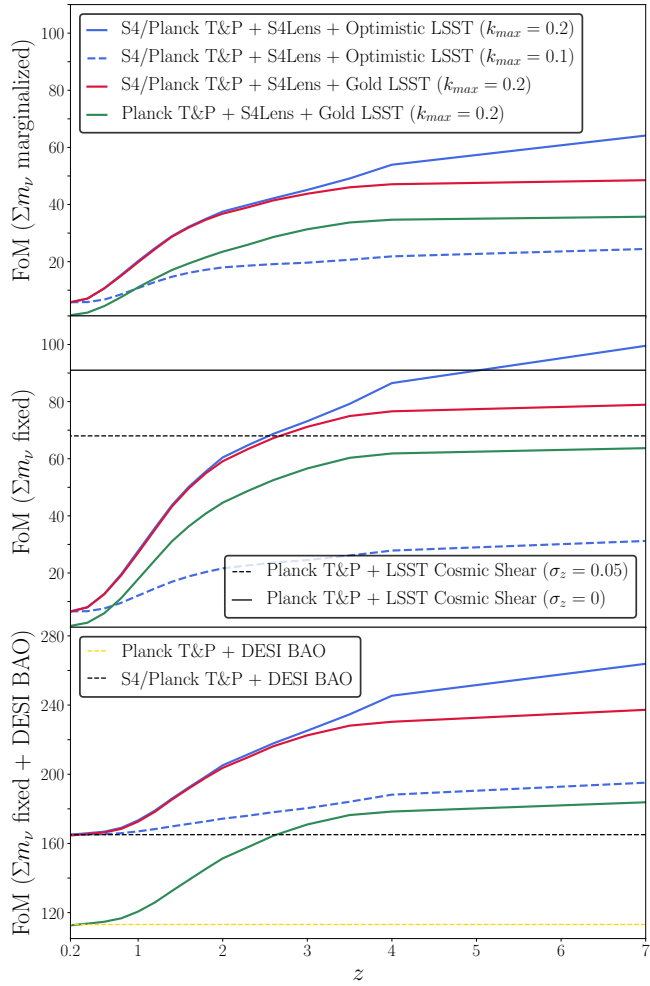


**Figure 5.** Forecasted DETF Figure of Merit for different experiment configurations and  $k_{\max}$  limits. *Top:* Forecasts with the neutrino mass sum marginalized. Addition of galaxy bins at higher redshift extends the redshift lever arm, resulting in a greater constraining power. *Middle:* Forecasts with the neutrino mass sum fixed. Our results are at a similar level to the forecast with LSST weak lensing combined with Planck measurements (Zhan 2006) (black). *Bottom:* Forecasts with the DESI BAO measurements included. With the S4 primary CMB data, we gain a noticeable improvement in forecasts relative to the Planck data.

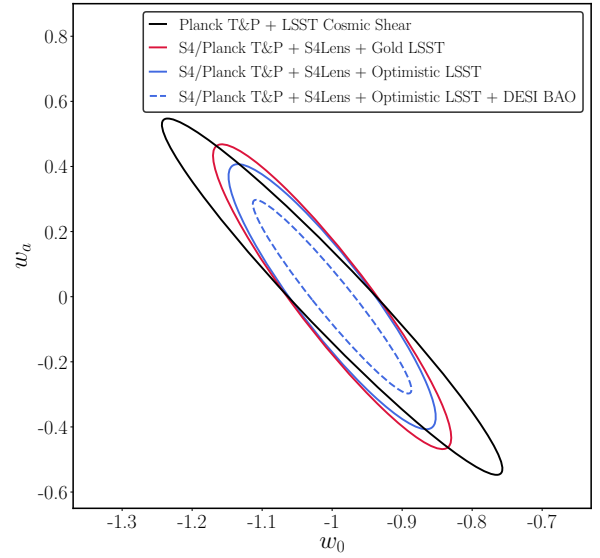


**Figure 6.**  $1\sigma$  confidence ellipses in the  $w_0 - w_a$  plane, with different survey configurations. We observe that dark energy constraints from LSST clustering in combination with CMB-S4 lensing (blue and red) are comparable to those from the LSST cosmic shear data (black).

bias function of  $b(z) = 1+0.84z$ , whereas we use  $1+z$ . The differences in  $\bar{n}$ ,  $f_{sky}$ , and  $b(z)$  should each affect the values of the FoM, but only to a small degree. Changing our forecast parameters to more closely match Zhan (2006)'s would change our forecasted FoM values somewhat.

As an alternative way to compare our forecasts with the LSST cosmic shear forecast, we also present  $1\sigma$  error ellipses in the  $w_0 - w_a$  plane. Figure 6 includes our forecasts with different survey configurations (assuming  $k_{\max} = 0.2h\text{Mpc}^{-1}$ ), for both the LSST Gold and Optimistic samples. Plotted with them is the LSST cosmic shear forecast from Zhan & Tyson (2018), and this includes anticipated systematics, such as additive and multiplicative errors in the shear power spectra and uncertainty in the photometric redshift error distribution. This forecast is similar to the one in Zhan (2006), though the LSST data model is updated, but it does not include galaxy clustering power spectra nor galaxy-galaxy lensing power spectra. Its error ellipsis appears to have a similar size as our forecast ellipses, consistent with the result shown in Figure 5.

## 5 SUMMARY

We have studied the prospect for CMB Lensing Tomography to constrain the dark energy parameters by combining LSST redshift-binned galaxy clustering maps and CMB-S4 convergence map. Although one might expect that the dominant contribution to dark energy constraints would come from the determination of the matter power spectrum as a function of redshift, the observable statistical properties that we consider (auto- and cross-power spectra) are also sensitive to the distance-redshift relation. We find that a comparable amount of information about  $w(a)$  comes from geometrical features as comes from growth.

To conduct such analysis, we need to take care not to artificially break degeneracies of galaxy biasing with the amplitude of the matter power spectrum. This danger is present due to the low dimensionality of our parameterization of the bias-redshift relation. In our analysis, we use one parameter for each bin, with a precisely fixed and known redshift dependence within each bin. To avoid an artificial breaking of degeneracy, we remove variation of the redshift dependence of  $P(k, z)$  within a redshift bin. As the dark energy equation of state parameters vary, we adjust the amplitude of  $P(k, z)$  at the center of each redshift bin, while keeping the shape unchanged.

We find that large angular scales are particularly important for the study of dark energy. Uncertainties associated with non-linear evolution and galaxy biasing on small scales lead us to ignore, in our forecasting, wavenumbers larger than  $k=0.2$   $h/\text{Mpc}$ . Another approach would be to increase the maximum  $k$  value as redshift increases, since the scale of non-linearity moves out to higher  $k$ . However, at higher redshift, the mean bias factor of the galaxies in the catalog increases, reducing tolerance to errors in the modeling of galaxy bias (Modi et al. 2017). The choice of fixed maximum  $k$  means that there is effectively a maximum value of  $l$  for each redshift bin, which is an increasing function of redshift.

Finally, we present the DETF Figure of Merit for different experiment configurations and find that adding CMB lensing information to LSST clustering increases the FoM by roughly a factor of 3-4. We also show that our result is comparable to those from LSST tomographic cosmic shear, suggesting that the combination of CMB-S4 lensing and LSST clustering is a competitive probe of dark energy with very different systematics, and therefore highly complementary to the traditional analyses.

## ACKNOWLEDGEMENTS

We had very useful conversations with Emanuele Castorina, Enea Di Dio, Emmanuel Schaan, Marcel Schmittfull and J. Anthony Tyson. SF acknowledges support from the Miller Institute at UC Berkeley, the Berkeley Center for Cosmological Physics and the Physics Division at Lawrence Berkeley National Laboratory while this work was being completed. LK's work was supported in part by NSF award 20010015 and by the U.S. Department of Energy Office of Science. We acknowledge use of the publicly available CAMB Python wrapper <https://camb.info/> (2021); <http://camb.readthedocs.io/en/latest/> (2021); Lewis et al. (2000) and QUICKLENS <https://github.com/dhanson/quicklens> (2017); Ade et al. (2016).

## DATA AVAILABILITY

The data underlying this article will be shared on reasonable request to the corresponding author.

## REFERENCES

- Abazajian K. N., Dodelson S., 2003, *Physical Review Letters*, 91, 041301  
 Abazajian K. N., et al., 2016, arXiv preprint arXiv:1610.02743  
 Abell P. A., et al., 2009, *Lsst science book*, version 2.0. arXiv:0912.0201  
 Ade P., et al., 2016, *Astronomy & Astrophysics/Astronomie et Astrophysique*, 594  
 Albrecht A., et al., 2006, arXiv preprint astro-ph/0609591  
 Barboza Jr. E. M., Alcaniz J. S., 2008, *Phys. Lett. B*, 666, 415  
 Bassett B. A., Fantaye Y., Hlozek R., Kotze J., 2011, *International Journal of Modern Physics D*, 20, 2559  
 Bean R., Doré O., 2004, in *AIP Conference Proceedings*. pp 88–95  
 Bleem L. E., et al., 2012a, *Astrophys. J.*, 753, L9  
 Bleem L., et al., 2012b, *The Astrophysical Journal Letters*, 753, L9  
 Chen S.-F., Lee H., Dvorkin C., 2021, *JCAP*, 05, 030  
 Chevallier M., Polarski D., 2001, *Int. J. Mod. Phys. D*, 10, 213  
 Colgáin E. O., Sheikh-Jabbari M. M., Yin L., 2021, *Phys. Rev. D*, 104, 023510  
 Cooray A., Hu W., 2000, *The Astrophysical Journal*, 534, 533  
 Crocce M., et al., 2015, *Monthly Notices of the Royal Astronomical Society*, 455, 4301  
 Darwish O., et al., 2021, *MNRAS*, 500, 2250  
 Efstathiou G., 1999, *Mon. Not. Roy. Astron. Soc.*, 310, 842  
 Eifler T., et al., 2021, *MNRAS*,  
 Fang X., Eifler T., Schaan E., Huang H.-J., Krause E., Ferraro S., 2021, preprint (arXiv:2108.00658)  
 García-García C., Ruiz Zapatero J., Alonso D., Bellini E., Ferreira P. G., Mueller E.-M., Nicola A., Ruiz-Lapuente P., 2021, arXiv e-prints, p. arXiv:2105.12108  
 Giannantonio T., et al., 2016, *Monthly Notices of the Royal Astronomical Society*, 456, 3213  
 González-Nuevo J., et al., 2017, *Journal of Cosmology and Astroparticle Physics*, 2017, 024  
 Hang Q., Alam S., Peacock J. A., Cai Y.-C., 2021, *MNRAS*, 501, 1481  
 Hannestad S., Tu H., Wong Y. Y., 2006, *Journal of Cosmology and Astroparticle Physics*, 2006, 025  
 Hartlap J., Hilbert S., Schneider P., Hildebrandt H., 2011, *Astronomy & Astrophysics*, 528, A51  
 Hildebrandt H., et al., 2016, *Monthly Notices of the Royal Astronomical Society*, 465, 1454  
 Hirata C. M., Seljak U., 2003, *Physical Review D*, 68, 083002  
 Hu W., Okamoto T., 2002, *The Astrophysical Journal*, 574, 566  
 Jassal H. K., Bagla J. S., Padmanabhan T., 2005, *Phys. Rev. D*, 72, 103503  
 Joudaki S., Kaplinghat M., 2012, *Physical Review D*, 86, 023526  
 Kaiser N., 1992, *The Astrophysical Journal*, 388, 272  
 Kaplinghat M., Knox L., Song Y.-S., 2003, *Physical Review Letters*, 91, 241301  
 Kitanidis E., White M., 2021, *MNRAS*, 501, 6181  
 Knox L., Song Y.-S., Tyson J. A., 2006, *Physical Review D*, 74, 023512  
 Krause E., Eifler T., 2017, *MNRAS*, 470, 2100  
 Krolewski A., Ferraro S., Schlafly E. F., White M., 2020, *J. Cosmology Astropart. Phys.*, 2020, 047  
 Krolewski A., Ferraro S., White M., 2021a, preprint (arXiv:2105.03421)  
 Krolewski A., Ferraro S., White M., 2021b, arXiv e-prints, p. arXiv:2105.03421  
 Lewis A., Challinor A., Lasenby A., 2000, *The Astrophysical Journal*, 538, 473  
 Limber D. N., 1953, *The Astrophysical Journal*, 117, 134  
 Linder E. V., 2003, *Phys. Rev. Lett.*, 90, 091301  
 Marques G. A., Bernui A., 2020, *Journal of Cosmology and Astroparticle Physics*, 2020, 052  
 Matilla J. M. Z., Haiman Z., Petri A., Namikawa T., 2017, *Physical Review D*, 96, 023513  
 Mishra-Sharma S., Alonso D., Dunkley J., 2018, arXiv preprint arXiv:1803.07561  
 Modi C., White M., Vlah Z., 2017, *J. Cosmology Astropart. Phys.*, 8, 009  
 Namikawa T., Saito S., Taruya A., 2010, *Journal of Cosmology and Astroparticle Physics*, 2010, 027  
 Omori Y., et al., 2018, arXiv e-prints, p. arXiv:1810.02342



- Pandey S., et al., 2021, preprint ([arXiv:2105.13545](https://arxiv.org/abs/2105.13545))
- Pen U.-L., 2004, Monthly Notices of the Royal Astronomical Society, 350, 1445
- Planck Collaboration et al., 2014, *A&A*, 571, A17
- Planck Collaboration et al., 2018, preprint, ([arXiv:1807.06210](https://arxiv.org/abs/1807.06210))
- Santos L., Cabella P., Balbi A., Vittorio N., 2013, Physical Review D, 88, 043505
- Schaan E., Krause E., Eifler T., Doré O., Miyatake H., Rhodes J., Spergel D. N., 2017, Physical Review D, 95
- Schaan E., Ferraro S., Seljak U., 2020, *JCAP*, 12, 001
- Schmittfull M., Seljak U., 2017, arXiv preprint arXiv:1710.09465
- Sherwin B. D., et al., 2012, *Phys. Rev.*, D86, 083006
- Simpson F., Bridle S., 2005, Physical Review D, 71, 083501
- Smith K. M., Hanson D., LoVerde M., Hirata C. M., Zahn O., 2012, Journal of Cosmology and Astroparticle Physics, 2012, 014
- Song Y.-S., Cooray A., Knox L., Zaldarriaga M., 2003, *Astrophys. J.*, 590, 664
- Takada M., Hu W., 2013, *Phys. Rev. D*, 87, 123504
- Tegmark M., Taylor A. N., Heavens A. F., 1997, The Astrophysical Journal, 480, 22
- Unnikrishnan S., et al., 2014, in Journal of Physics: Conference Series. p. 012048
- Wu W., Errard J., Dvorkin C., Kuo C., Lee A., McDonald P., Slosar A., Zahn O., 2014, The Astrophysical Journal, 788, 138
- Yu B., Knight R. Z., Sherwin B. D., Ferraro S., Knox L., Schmittfull M., 2018, <https://arxiv.org/abs/1809.02120>
- Zhan H., 2006, Journal of Cosmology and Astroparticle Physics, 2006, 008
- Zhan H., Knox L., 2006, arXiv preprint astro-ph/0611159
- Zhan H., Tyson J. A., 2018, Reports on Progress in Physics, 81, 066901
- Zhan H., Knox L., Tyson J. A., 2008, The Astrophysical Journal, 690, 923
- Zhang J., Hui L., Stebbins A., 2005, The Astrophysical Journal, 635, 806  
<http://camb.readthedocs.io/en/latest/> 2021  
<https://camb.info/> 2021  
<https://github.com/dhanson/quicklens> 2017

This paper has been typeset from a  $\text{\TeX}/\text{\LaTeX}$  file prepared by the author.